SYNTHESIS OF Cr-DOPED $SrMoO_4$ WITH ENHANCED PHOTOCATALYTIC PERFORMANCE VIA HYDROTHERMAL METHOD

L. Y. ZHANG[a,b,*], A. B. ZHANG[a], G.H. ZHENG[b,c], Z. X. DAI[b], W. YANG[a]
[a]*School of Energy Materials and Chemical Engineering, Hefei University, Hefei 230601, China*
[b]*Key Laboratory of Structure and Functional Regulation of Hybrid Materials (Anhui University), Ministry of Education, Hefei, 230601, China*
[c]*Anhui Key Laboratory of Information Materials and Devices, School of Physics and Materials Science, Anhui University, Hefei 230039, China*

Cr-doped $SrMoO_4$ visible-light-driven photocatalysts were successfully synthesized by one-pot facile hydrothermal technique. The results show that Cr doping slightly affected the crystal structure of $SrMoO_4$. However, Cr doping plays an important role in sample morphology. Photocatalytic properties were evaluated by the degradation of methyl blue under visible-light irradiation. Electron spin resonance measurements show that the $\bullet O_2^-$ radical is the major active species in photodegradation. Photocatalytic measurement results indicate that Cr^{3+} doping effectively increases the photocatalytic activity of $SrMoO_4$. When the Cr doping is 7%, the doped $SrMoO_4$ exhibits the best photocatalytic performance. The increase in photocatalytic activity can be attributed to the following two factors: One is the decrease in sample band gap, and the other is the lower recombination ratio of photoinduced electron–hole pairs with Cr doping. The current experimental results clearly indicate that Cr doping is a useful method to improve the photocatalytic properties of $SrMoO_4$ material.

(Received November 11, 2020; Accepted March 10, 2021)

Keywords: Synthesis, SrMoO4, Cr-doped, Hydrothermal method, Photocatalyst

1. Introduction

For the elimination of hazardous pollutants, photocatalysis is one of the most promising technologies in the past decades. The catalyst plays an important role in photocatalytic reaction and affects the reaction efficiency significantly. Many types of catalysts have been studied [1–3]. Among these various types of photocatalysts, scheelite-structured $AMoO_4$ (A = Sr, Ba, Ca, Pb) molybdates have attracted much attention in recent year [4–8]. Many studies have demonstrated that some of these molybdates such as $PbMoO_4$ [9], $CdMoO_4$ [10], and $CaMoO_4$ [11] have remarkable photocatalytic activity for the degradation of organic pollutants despite their relatively larger band-gap energies.

* Corresponding author: 522671714@qq.com

$SrMoO_4$, one of the representative scheelite-structured molybdates, has a tetragonal crystal symmetry with the space group I41/a [12]. Each Mo site is surrounded by four equivalent O sites in an almost tetrahedral configuration; each Sr site is surrounded by eight O sites in an almost octahedral configuration. The primitive unit cell has two $SrMoO_4$ units, and each unit has an inversion center. Because of the interactions between Mo *d* and O *2p* orbitals with some covalent contribution to ionic bonds, $SrMoO_4$ is regarded as a semiconductor material with a wide band gap (4.0 eV) [13]. Therefore, $SrMoO_4$ absorbs only UV light, and the photocatalytic activity is not excellent. The entire solar light is composed of ~3% UV light, 52% visible light, and 45% near-infrared light. To fully utilize the solar energy and increase the photocatalytic activity of $SrMoO_4$, many methods have been developed. Wang et al. [14] synthesized Bi^{3+}-doped $SrMoO_4$ nanocrystals using a simple hydrothermal method; the photocatalytic performance increased significantly. By changing the stirring process in the hydrothermal preparation, the photodegradation of methyl blue (MB) over $SrMoO_4$ system increased from 30% to 50% when the stirring speed increased from 0 to 200 rpm [15].

The doping or replacement of one foreign element in active photocatalysts with wide band gaps is one of the effective methods to increase the photocatalytic performance. Zhou et al. ascribed the increase in photocatalytic activity of $BiVO_4$ with M doping (M = Ag, Co, and Ni) to the decrease in the recombination of photogenerated electrons and holes owing to the formation of hybrid metal oxides [16]. The doping of Cr^{3+} ions to TiO_2 and $SrTiO_3$ increases the photocurrent of semiconductor and photocatalytic decomposition of organic compounds. It was assumed that an isolated acceptor level derived from Cr *3d* orbitals existed between the conduction band (CB) and valence band (VB) with Cr ion substitution into $SrMoO_4$ photocatalyst. As a result, the photocatalytic activity is affected [17,18]. Based on the above ideas, in this study, Cr-doped $SrMoO_4$ catalysts were synthesized by a facile hydrothermal method. In the following text, these Cr-doped $SrMoO_4$ samples are labeled as Cr/$SrMoO_4$ for simplification. Some interesting results were obtained. Photocatalytic experiments showed that the Cr/$SrMoO_4$ photocatalytic activity for MB degradation increased with the introduction of Cr under visible-light irradiation. The results indicate that for $SrMoO_4$ system, Cr doping is an important method to improve the photocatalytic properties. A possible mechanism is also proposed based on these experimental results.

2. Experimental

2.1. Synthesis of materials

Stoichiometric amounts of $Sr(NO_3)_2$, $Cr(NO_3)_3$, $(NH_4)_6Mo_7O_{24}$, and NaOH were separately dissolved in deionized water under magnetic stirring for 20 min. Then, $Sr(NO_3)_2$ and $(NH_4)_6Mo_7O_{24}$ were mixed with continuous stirring. NaOH solution was added to adjust the pH. Finally, the mixture was added to a 1000-mL Hastelloy autoclave (Parr 4577) and reacted at 120 °C for 6 h. After the autoclave was naturally cooled to room temperature, the products were separated by centrifugation, washed with ethanol and deionized water several times, and subsequently dried at 80 °C to obtain the final samples. The obtained samples had different Cr dopings (0, 0.01, 0.03, 0.05, 0.07, 0.09, and 0.11). These samples are referred as Cr00, Cr001, Cr003, Cr005, Cr007, Cr009, and Cr011, respectively, in the following text.

2.2. Characterization

Crystal structures of the products were characterized by X-ray diffraction (XRD) using an X-ray diffractometer (dx-2000 SSC) with Cu *Kα* radiation (λ = 1.5418 Å) over a scanning range of 10–80° with a step of 0.02°. Scanning electron microscopy (SEM, S-4800, Hitachi) was used to observe the morphology and microstructure. X-ray photoelectron spectroscopy (XPS) was carried out using a Thermo Scientific ESCALAB 250Xi (ESCALAB 250Xi, Thermo Scientific Inc., USA). UV–vis absorbance spectra were measured using a Shimadzu UV-3600 (Japan) using $BaSO_4$ as the reference. The excitation and emission spectra were measured using a fluorescence spectrophotometer (F-4500, Hitachi). The electron spin resonance (ESR) studies were performed using a continuous-wave X-band ESR spectrometer (Bruker EMX plus 10/12) at room temperature with the signals of radicals trapped by 5,5-dimethyl-1-pyrroline *N*-oxide (DMPO). The microwave frequency was 9.39 GHz for all the performed measurements, and the applied field H was swept up to 14 KOe.

The photocatalytic activity of $Cr/SrMoO_4$ samples was evaluated by the degradation of MB under 350-W Xe lamp light irradiation. In each experiment, 200 mg of the photocatalyst was added to 80 mL of MB solution (10 mg/L) in one test tube. Before the illumination, the suspensions were magnetically stirred in the dark for 1 h to reach the adsorption–desorption equilibrium between the photocatalyst and MB solution. Then, the solution under magnetic stirring was exposed to Xe-lamp light irradiation. At a given interval time, the test tubes were sampled and then centrifuged to remove the photocatalyst particles.

3. Results and discussion

3.1. XRD analysis

For all these obtained samples, the XRD patterns were carefully measured, as shown in Fig. 1. The results indicate that the XRD patterns did not change with Cr doping to $SrMoO_4$. The sharp and well-defined peaks indicate that these samples crystallized well, and no other impurity is present. The observed pattern indicates that all the prepared $SrMoO_4$ samples have a pure scheelite tetragonal structure (I41/a space group), corresponding to JCPDS 850586. The diffraction peaks of the as-prepared samples correspond to the (101), (112), (004), (200), (211), (204), (220), (116), (303), and (224) planes, as shown in Fig. 1. The XRD results indicate that Cr was successfully introduced into the $SrMoO_4$ host lattice.

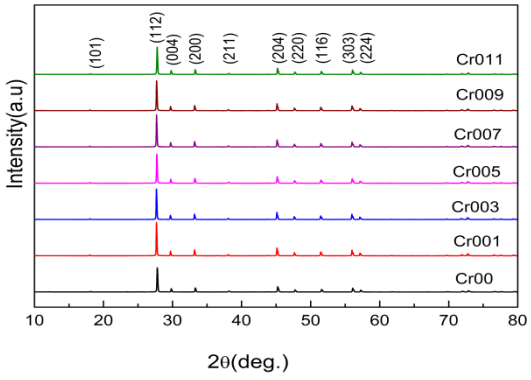

Fig. 1. XRD pattern for all Cr-$SrMoO_4$ samples.

As mentioned above, in $SrMoO_4$ lattice, each central Mo atom is surrounded by four equivalent O atoms, constituting one MoO_4^{2-} tetrahedral symmetry configuration. Each divalent metal atom shares corners with eight adjacent O atoms in MoO_4^{2-} tetrahedron [19]. The lattice parameters of these obtained five samples were calculated using $\frac{1}{d^2}=\frac{h^2+k^2}{a^2}+\frac{l^2}{c^2}$, where $2d\sin\theta=n\lambda$; a and c are the lattice parameters; θ is the diffraction angle; λ is the wavelength of Cu Kα irradiation; (h k l) are the crystal plane indexes. The calculated lattice parameters are shown in Table 1. The lattice parameters of these samples changed slightly with the increase in Cr doping. The crystallite size was calculated using the Scherrer's formula: $D=\frac{K\lambda}{\beta\cos\theta}$, where D is the crystal size; λ is the wavelength of X-ray radiation (λ = 0.15406 nm), K is a constant at 0.89, β is the peak width of half-maximum height of (1 1 2) of the sample [20]. The calculated average crystallite sizes of pure and Cr-doped $SrMoO_4$ samples are shown in Table 1. The least variation in lattice parameters and crystallite size indicate that the slight distortions can be attributed to the slight difference in ion sizes between Cr (r = 0.615 Å) and Mo (r = 0.59 Å), as discussed below.

Table 1. The lattice parameters, Crytallite size, and Eg value for all samples.

Sample	Cr00	Cr001	Cr003	Cr005	Cr007	Cr009	Cr011
a (Å)	5.3834	5.3857	5.3776	5.3774	5.3783	5.3772	5.3803
c (Å)	11.9553	12.0120	12.0293	12.0415	12.0355	12.0404	12.0418
Crytallite size(nm)	40.3	42.1	41.8	42.9	43.6	47.9	50.3
Eg(eV)	3.97	3.97	3.93	3.85	3.83	3.87	3.93
E_{VB}(eV)	2.90	2.90	2.88	2.84	2.83	2.85	2.88
E_{CB}(eV)	-1.07	-1.07	-1.05	-1.01	-1.00	-1.02	-1.05

3.2. XPS analysis

The surface chemical composition and chemical states of Cr-doped $SrMoO_4$ were analyzed by XPS. The XPS patterns of Cr, Sr, Mo, and O for pure $SrMoO_4$ (Cr00) and 5% Cr-$SrMoO_4$ (Cr005) are shown in Figure 2.

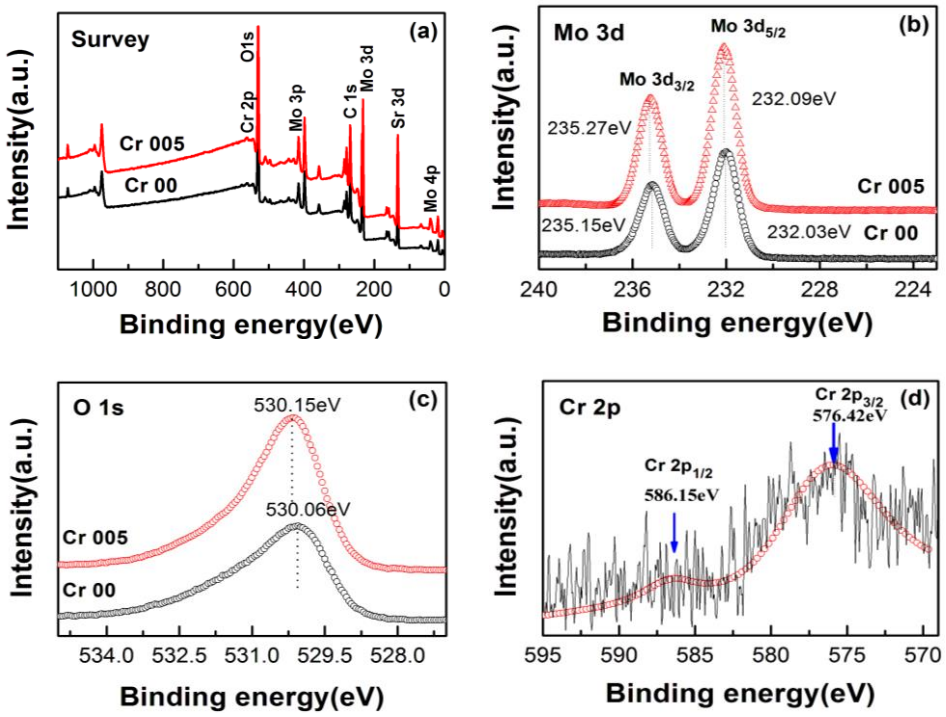

Fig. 2. Survery (a), Mo 3d (b), O1s (c) XPS spectra for Cr00 and Cr005 samples; (d) Cr 2p XPS spectra for Cr005 sample.

The peaks corresponding to Mo 4p, Mo 3d, Mo 3p, and Sr 3d, O 1s were clearly detected in both the samples. The binding peaks of C 1s were observed at 284.6 V, originating from the C in the instrument. In addition, one weak peak of Cr appeared at ~575.83 eV in the Cr005 sample, as shown in Fig. 2(a). Fig. 2(b) shows the high-resolution XPS spectrum of Mo. These peaks centered at 235.15 (235.27) eV and 232.03 (232.09) eV are assigned to Mo $3d_{3/2}$ and Mo $3d_{5/2}$, respectively. Notably, the binding energies of Mo $3d_{3/2}$ and Mo $3d_{5/2}$ in the current doped samples are not similar to those of pure $SrMoO_4$ sample (235.1 and 232.2 eV) [21]. This indicates that both the local environment and electron density of Mo changed with Cr doping. Fig. 2(c) shows the high-resolution XPS spectrum of O 1s for both the samples. The peaks at binding energies of 530.06 eV for pure $SrMoO_4$ and 530.15 eV for 5%Cr-doped $SrMoO_4$ correspond to O 1s, as shown in Figure 2(c). To further identify the chemical state of Cr, the Cr 2p high-resolution XPS spectrum of 5%Cr-doped $SrMoO_4$ is shown in Figure 2(d). Cr $2p_{1/2}$ and Cr $2p_{3/2}$ are unimodal, and the binding energies are 586.15 eV and 576.42 eV, respectively. This indicates that Cr exists in the form of Cr^{3+} [22]. The radius of Cr^{3+} (0.615 Å) is much smaller than Sr^{2+} (1.18 Å), but it is almost similar to the radius of Mo^{6+}(0.59 Å). Therefore, it is reasonable to conclude that in the internal lattice structure of $SrMoO_4$, some Mo^{6+} ions are replaced with Cr^{3+} dopant.

The XPS results show that the concentrations of surface Sr^{2+} and Mo^{6+} are 13.21 atom% and 12.69 atom% for 5% Cr-doped sample, respectively. Thus, it can be concluded that the corresponding atomic ratio of Sr and Mo is ~1.04. The atomic ratio of Sr and Mo is larger than that of the stoichiometric ratio of $SrMoO_4$, indicating that Cr doping occurs at the Mo site of the

sample. The radius of Cr (0.615 Å) is similar to that of Mo (0.590 Å); therefore, no shift occurred in the diffraction pattern.

3.3. SEM analysis

Figs. 3(a–f) show the SEM profiles of all the samples Cr001, Cr003, Cr005, Cr007, Cr009, and Cr011, respectively.

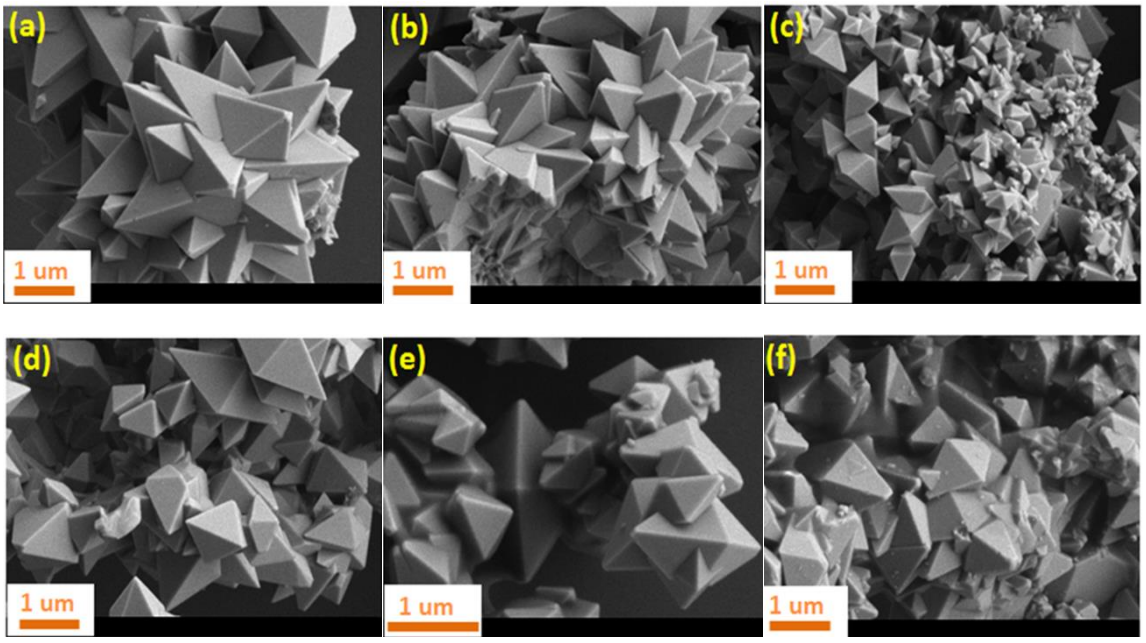

Fig. 3. SEM for Cr00(a), Cr003(b), Cr005(c), Cr007(d), Cr009(e), Cr011(f) samples.

Cr/$SrMoO_4$ powders show a large quantity of anisotropic microcrystals with octahedron-like morphology. Several methods are available to prepare $SrMoO_4$ samples, such as co-precipitation reaction, microwave radiation, electrochemical process, hydrothermal method, and sol–gel method [23–26]. Various morphologies such as flower-like sphere, spindle rod, peanut, dumbbell, hierarchical nanosheets, nanowires, and nanoplates have been obtained [27,28]. The SEM results are completely different from those reported in previous studies. Obviously, Cr doping significantly affects $SrMoO_4$ morphology. The morphologies of Cr/$SrMoO_4$ with scheelite-type structure are faceted and aligned by "docking" processes, creating an extended morphology as shown in Fig. 3 **[**29].

3.4. Optical properties

Fig. 4 shows the photoluminescence (PL) properties of the obtained samples. In the measurement process, an excitation wavelength of 217 nm was used. One broad emission peak appeared at 365 nm in the wavelength range 300–400 nm. A clear blue-green emission band centered at 473 nm was observed. This band is probably directly related to the charge transfer within the [MoO_4^{2-}] tetrahedral group [30,31]. In addition, one weak green emission was observed at ~550 nm. Similar phenomenon were also observed in other studies [32,33]. Obviously, with Cr

doping to $SrMoO_4$, the emission center did not change. However, the PL intensities first decreased and then increased, as shown in Figure 4. Generally, the PL spectra of semiconductor materials are widely used as an effective technique to determine the migration, transfer, and recombination processes of photogenerated electron–hole pairs stimulated under light illumination. A higher PL intensity usually indicates a lower separation efficiency of photoinduced electron–hole pairs and lower photocatalytic performance. Clearly, the emission intensity of pure $SrMoO_4$ is the highest, i.e. the photogenerated electrons and holes of $SrMoO_4$ recombine easily. With Cr doping, the relative PL intensity decreased. This indicates that the recombination of electrons and holes decreased with Cr^{3+} doping. Moreover, the intensities of PL spectra for $SrMoO_4$ decreased with increasing Cr^{3+} content and reached the minimum when the Cr^{3+} content is 7%. With further increase in Cr^{3+}, the emission intensities of PL spectra increased. These results indicate that 7% Cr^{3+} doping effectively restrains the recombination of photoinduced electrons and holes. The photoluminescence results are consistent with the photocatalytic activities in the following section. $SrMoO_4$ is comprised of $[MoO_4]^{2-}$ anions and Sr^{2+} cations. The strength of Mo–O covalent bonds in $[MoO_4]^{2-}$ anions is strong, and the coupling between $[MoO_4]^{2-}$ anions and Sr^{2+} cations is weak. In addition, the Mo 4*d*(t_{2g}) and Mo 4*d*(e_g) orbitals for $SrMoO_4$ are hybridized with the O 2*p*(σ) and O 2*p*(π) ligand orbitals to form $[MoO_4]^{2-}$ tetrahedrons. Generally, the emission is affected by charge transfer between different energy states within the MoO_4^{2-} tetrahedral groups as well as the structural arrangement. The XRD results indicate that with Cr doping into $SrMoO_4$ lattice, the lattice parameters changed, and the $[MoO_4]$ tetrahedral is distorted. This distortion can induce changes in the photoluminescence properties and photocatalytic activities.

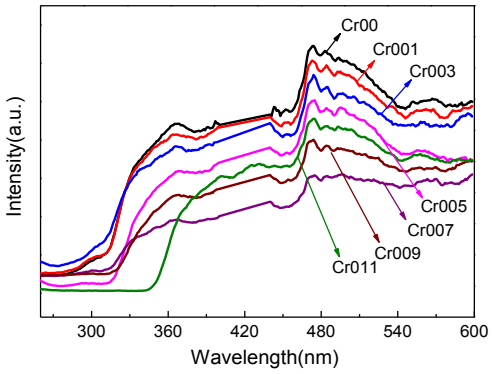

Fig. 4. Photoluminescence spectra of all samples excited with 217 nm.

UV–visible absorption spectra of Cr00, Cr001, Cr003, Cr005, Cr007, Cr009, Cr011 products were measured, and the results are shown in Fig. 5. Clearly, these samples showed strong absorption in the UV region. Moreover, one broad absorption band was observed between 200 nm and 400 nm. This board absorption band can be attributed to charge transfer from the oxygen (2*p*) electrons to the central Mo atom inside the $[MoO_4]^{2-}$ ion. The optical band gap energy (Eg) was also calculated using the method proposed by Wood and Tauc [34]. The optical band gap is related to the absorbance and photo energy by the following equation: $\alpha h\nu = A(h\nu - E_g)^n$, where α, h, ν, E_g, and A are the absorption coefficient, Planck constant, photon frequency, photonic energy gap, and a constant, respectively. In this equation, n is a constant associated with different types of

electronic transitions. Generally, n = 1/2, 2, 3/2, or 3 for directly allowed, indirectly allowed, directly forbidden, and indirectly forbidden transitions, respectively. According to Lacomba-Perales et al. [35], molybdates with scheelite-type tetragonal structure show one directly allowed electronic transition. Thus, in this study, n = 1/2 was used as the standard value in the above equation. For n = 1/2, the energy gap E_g values can be determined by extrapolating the linear portion of plot $(\alpha h\nu)^2$ vs. $h\nu$ to zero absorbance. Accordingly, the calculated energy gaps of Cr00, Cr001, Cr003, Cr005, Cr007, Cr009, and Cr011 samples are 3.97, 3.97, 3.93, 3.85, 3.83, 3.87, and 3.93 eV, respectively. The calculated *E*g for Cr00 sample is close to the value reported previously [36]. Obviously, Eg first decreases and then increases with Cr doping. When Mo^{6+} ion was substituted with Cr^{3+}, intermediate levels were introduced within the band gap. At the same time, Muralidharan [37] reported that with Cr injection into $SrSnO_4$, paramagnetic (PM) to ferromagnetic (FM) phase transition occurs. The ferromagnetic phase originates from the possible interaction between Cr 2p state and Sn 3d state. Moreover, this type of FM interaction is beneficial for electron hopping. This is probably another reason for the decrease in the band gap. However, with increasing Cr doping to 0.09 and 0.11, the antiferromagnetism interaction between Cr^{3+} and Cr^{3+} in Cr-doped $SrSnO_4$ system may form. As a result, the Eg increases. Compared with pure $SrSnO_4$, the narrower band gap of Cr-doped $SrSnO_4$ system decreases the recombination rate of photogenerated electron–hole pairs and correspondingly increases the photocatalytic activities, as discussed below.

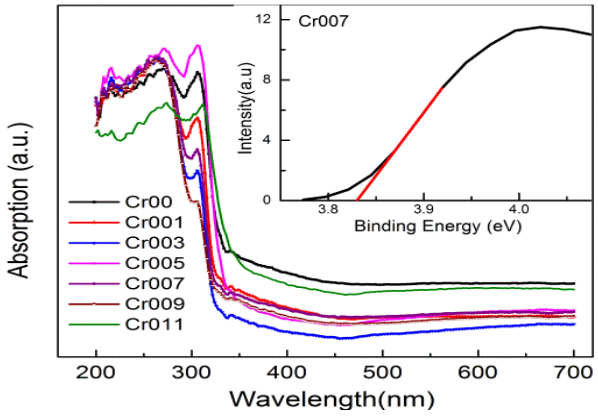

Fig. 5. UV-vis diffuse reflectance spectra for all samples, Inset plots of $(\alpha h\nu)^2$ vs photo energy (hv) for Cr007 sample.

The VB and CB positions can be obtained using the following formula:

$$E_{VB} = X - E_e + 0.5E_g$$
$$E_{CB} = E_{VB} - E_g$$

where E_{VB} is the VB potential and E_{CB} is the CB potential. X is the electronegativity of semiconductor, the geometric mean of the electronegativity of constituent atoms. Ee is the energy of free electrons on the hydrogen scale (4.50 eV), and Eg is the bandgap energy of semiconductor.

X for $SrMoO_4$ is 5.415. The VBs E_{VB} and conducting band E_{CB} positions of $SrMoO_4$ were calculated, and they are shown in Table 1.

3.5. ESR analysis

To further investigate the active species of photocatalysts, room-temperature ESR measurements were carried out for Cr-doped $SrMoO_4$ system under simulated sun-light irradiation. In ESR studies, DMPO was used as the trapping agent.

Figure 6 shows the ESR signals of DMPO-•OH and DMPO-$•O_2^-$ of Cr00, Cr003, and Cr007 samples before and after light illumination. When the measurements are performed in dark conditions, no ESR signal was observed for all the samples. Moreover, week ESR signals of DMPO-•OH of Cr00 appeared upon light irradiation (Figure 6(a)), indicating that •OH is not the major oxidation species in this process [38]. However, with increasing Cr doping to 0.03 and 0.07, a quartet line profile with a 1:2:2:1 intensity pattern was observed, and at g = 2.004 with $a_N = a_H =$ 14.7 G, hyperfine splitting constants were observed. This is consistent with the spectra reported in the literature for the DMPO-•OH adduct and confirmed the formation of •OH radicals during the irradiation of Cr-doped $SrMoO_4$. One possible route of •OH production of Cr-$SrMoO_4$ is that the holes on the surface of Cr-$SrMoO_4$ can be trapped by adsorbed OH^- and H_2O to generate •OH [39]. Figure 6(b) shows that upon light illumination, ESR signals of DMPO-$•O_2^-$ appeared for Cr00, Cr003, and Cr007 samples. Cr007 showed much stronger ESR signals than Cr00. Moreover, The signal intensity of $•O_2^-$ is higher than that of •OH, i.e., the $•O_2^-$ radical is the major active species in photodegradation. Consequently, it can be inferred that both the holes (h^+) and superoxide radicals ($•O_2^-$) play a crucial role in the photocatalytic oxidation for Cr-doped $SrMoO_4$ [40,41].

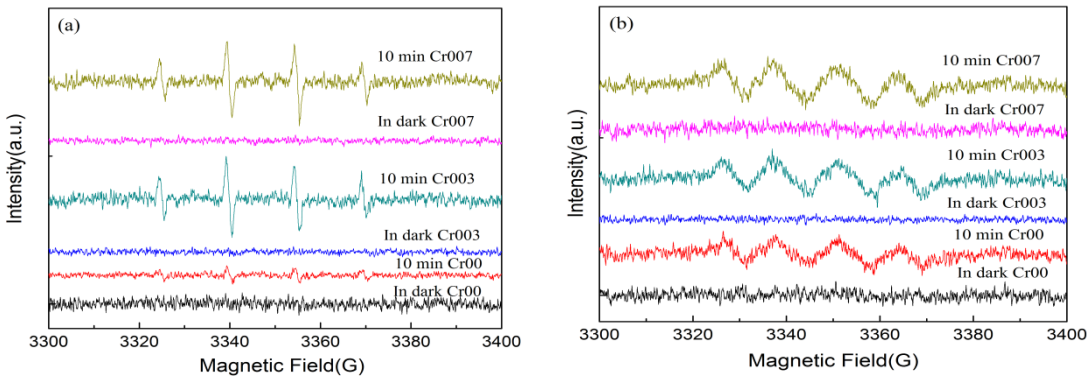

Fig. 6. DMPO spin-trapping ESR spectra of Cr00, Cr003 and Cr007 samples: (a) in an aqueous dispersion for DMPO-•OH and (b) in a methanol dispersion for DMPO-$•O_2^-$.

3.6. Photocatalytic properties

The photocatalytic activities of as-prepared Cr-doped $SrMoO_4$ samples were evaluated by the degradation of MB dye under visible-light irradiation at room temperature. Fig. 7 shows the temporal evolution of MB solution absorption spectra under visible-light irradiation for 11% Cr-doped $SrMoO_4$ sample (Cr011). It was decreased with the increase in irradiation time.

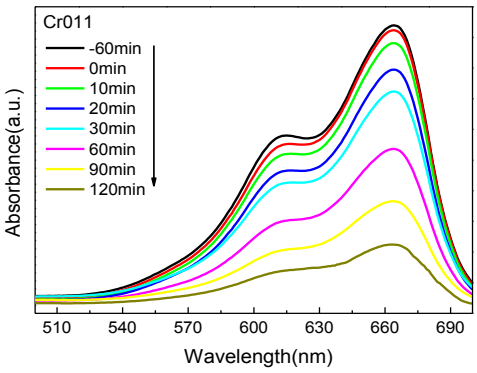

Fig. 7. Absorption spectra of MB with irradiation time over Cr011 sample.

Fig. 8 shows the variation in MB concentration (C/C_0) with irradiation time over these photocatalysts prepared with different amounts of Cr doping. The photodegradation rate of MB over pure $SrMoO_4$ is 64.8% after the irradiation for 120 min under the same conditions. With Cr doping in $SrMoO_4$, the photodegradation rates of MB were 75.5%, 84.6%, 86.7%, 92.1%, 89.2%, and 80.8% after the irradiation for 120 min for Cr001, Cr003, Cr005, Cr007, Cr009, and Cr011 samples, respectively. Therefore, these photocatalytic activities of $Cr/SrMoO_4$ samples are closely related to Cr doping concentration.

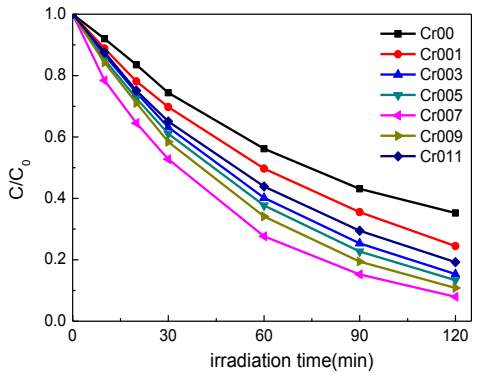

Fig. 8. The degradation rates of MB under visible-light irradiation the presence for all Cr-$SrMoO_4$ samples.

Obviously, all these doped samples exhibited a higher efficiency than the undoped sample. When the Cr concentration was increased from 0 to 7%, the photocatalytic activity gradually increased. With further increase in the doping content, the photocatalytic performance started to decrease. Therefore, 7% is the best doping content, and 7% Cr-doped $SrMoO_4$ (Cr007) shows the best degradation performance. In the case of 7% Cr content, 92.1% MB was degraded in 120 min, whereas pure $SrMoO_4$ degraded only 64.8% of MB within the same time. More interestingly, when the doping content was more than 7%, even though the photocatalytic activity gradually decreased, it was still better than that of pure $SrMoO_4$.

The kinetic behaviors of all samples for photodegradation of MB are plotted according to the pseudo- first- order kinetic model: $\ln(C_0/C) = kt$, where C_0 and C are initial concentration and instant concentration reaction time t, and k is the rate constant. The plot of $\ln(C_0/C)$~t exhibits a good linearity, as depicted in Fig. 9. Obviously, here the photocatalytic degradation of MB is accordance with the first- order kinetic model. The k value is 0.00905, 0.01167, 0.01542, 0.0166, 0.02113, 0.0183, and 0.01372 min^{-1} for Cr00, Cr001, Cr003, Cr005, Cr007, Cr009, and Cr011 samples, respectively. The k value over Cr007 sample (0.02113 min^{-1}) reaches to the maximal value and is about 2 times higher than that of Cr00 (0.00905 min^{-1}). The current experimental studies clearly indicate that Cr doping is a useful method to improve the photocatalytic properties of $SrMoO_4$. Moreover, a desirable doping content in $SrMoO_4$ system is also shown regarding MB photocatalytic degradation efficiency.

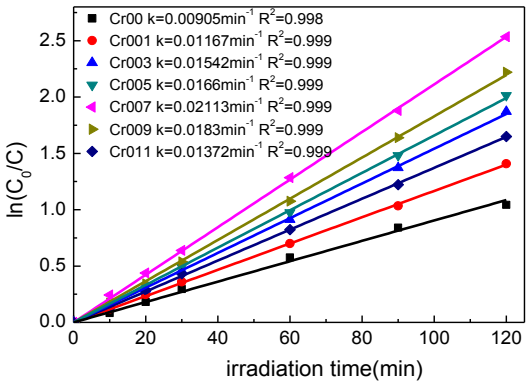

Fig. 9. The relationship between $\ln(C_0/C)$ and irradiation time t (min) for all Cr-$SrMoO_4$ samples.

A perfect photocatalyst should have one proper band gap to provide energetic electrons, separate photogenerated charge efficiently, and inhibit the photocorrosion process significantly [42,43]. Furthermore, a small band gap is also a necessary factor to allow efficient absorption overlap with the solar spectrum. It is very important for the photocatalyst to effectively utilize solar energy [44,45]. As discussed above, the UV–vis results indicate that the band gaps of the obtained samples decreased after Cr doping. Therefore, it is reasonable to conclude that the higher photocatalytic properties of these Cr-doped samples can be attributed to the smaller band gap.

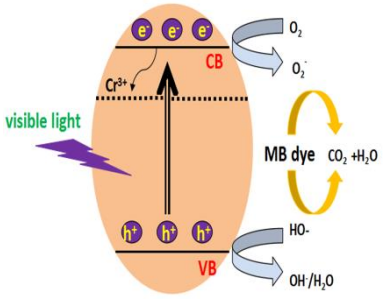

Fig. 10. Schematic diagram of charge carrier transfer process and possible photocatalytic mechanism of Cr-$SrMoO_4$ nanoparticles.

Second, in the case of visible-light irradiation, the Cr-$SrMoO_4$ photocatalyst is activated, and the electrons (e^-) in the VB are stimulated to the CB with the same number of holes (h^+) being left in the VB. The electrons are caught by O_2 adsorbed on the surface of Cr-doped $SrMoO_4$ acting as the active sites to produce $\bullet O_2^-$ superoxide radicals. Moreover, the photogenerated holes of VB can react with H_2O and OH^- to generate •OH hydroxyl radicals as strong oxidizing agents. When Cr is doped into $SrMoO_4$, the electrons on CB could be captured by trapping sites of Cr^{3+} ions, leading to an improved separation efficiency of photogenerated charge carriers. With increasing Cr content, more and more electrons and holes participated in the photocatalytic process, and a higher photodegradation rate for MB was achieved. However, when the amount of Cr^{3+} doping is higher than the optimum amount of doping, excessive Cr^{3+} may be the center of electron–hole pair recombination. Therefore, the photocatalytic activity decreased in the case of Cr009 and Cr011 samples. A plausible electron transfer and degradation mechanism of MB over $SrMoO_4$ is proposed, as shown in Figure 10.

The electrons in the CB of $SrMoO_4$ with strong reduction power react with the absorbed O_2 and produce superoxide anion radicals ($\bullet O_2^-$) that oxidize MB and provide a high photocatalytic degradation rate. Simultaneously, the VB holes remain on the Cr ion, and the VB of $SrMoO_4$ reacts with H_2O/OH^- to generate hydroxyl radical species (•OH) with strong oxidizing power. Then, the MB dye molecules are directly oxidized to CO_2, H_2O, and other small molecules. Cr doping decreases the recombination of photo-induced electrons and holes and prolongs the lifetime of electron pairs. As a result, the photocatalytic activity of $SrMoO_4$ material increased.

4. Conclusions

In this study, Cr-doped $SrMoO_4$ samples were successfully synthesized by hydrothermal method. The structure, micromorphology, luminescence properties, and photocatalytic properties were systematically evaluated. XRD patterns show the formation of a scheelite-type tetragonal structure; these XRD results also show that the host crystal structure does not change with Cr doping. The analysis of lattice parameter indicates that one slight distortion of [MoO_4] tetrahedron occurs with Cr doping into $SrMoO_4$. ESR measurements show that both the holes (h^+) and superoxide radicals ($\bullet O_2^-$) are the major active species in photodegradation.

The UV–vis absorption spectra show that the Eg of obtained samples decreased from 3.97 eV to 3.83 eV with Cr doping. This is associated with the presence of intermediary energy levels within the band gap. Cr doping increases the emission intensity. This can be ascribed to [MoO_4] distortion. The photodegradation efficiency of as-prepared samples was also evaluated by monitoring the degradation of MB under visible-light irradiation. The experimental results indicate that the photocatalytic activity increased with Cr doping. Further, 7% Cr-doped $SrMoO_4$ shows the optimal photocatalytic performance in the degradation of MB. The increase in photocatalytic activity can be attributed to the smaller band gap and introduction of intermediary energy levels. This decreases the recombination rate of photoinduced electrons and holes and prolongs the lifetime of carriers. This experimental study provides a useful technique to improve the photocatalytic performance of $SrMoO_4$ system.

Acknowledgments

This work was financially supported by the Open Project of Key Laboratory of Structure and Functional Regulation of Hybrid Materials (Anhui University), Ministry of Education, Key Research and Development Projects of Anhui Province (1804A09020096), and the Higher Educational Natural Science Foundation of Anhui Province (KJ2017A534).

References

[1] Y. L. Geng, P. Zhang, N. Li, Z. H. Sun, J. Alloy. Compd. **651**, 744 (2015).
[2] Y. I. Song, S. S. Hong, Res. Chem. Intermediat. **42**, 367 (2016).
[3] P. Wei, J. W. Liu, Z. H. Li, Ceram. Int. **39**, 5387 (2013).
[4] R. Z. Zhuang, G. F. Wang, Opt. Express **24**, 7543 (2016).
[5] S. K. Sharma, S. Dutta, S. Som, P. S. Mandal, J. Mater. Sci. Technol. **29**, 633 (2013).
[6] L. K. Bharat, S. H. Lee, J. S. Yu, Mater. Res. Bull. **53**, 49 (2014).
[7] B. K. Maji, H. Jena, R. Asuvathraman, K. V. G. Kutty, J. Alloy. Compd. **640**, 475 (2015).
[8] X. Y. Li, M. B. Dong, F. F. Hu, Y. G. Qin, L. Zhao, X. T. Wei, Y. H. Chen, C. K. Duan, M. Yin, Ceram. Int. **42**, 6094 (2016).
[9] S. Ganguli, C. C. Hazra, T. Samanta, V. Mahalingam, RSC Adv. **5**, 45611 (2015).
[10] J. H. Bi, Z. Y. Zhou, M. Y. Chen, S. J. Liang, Y. H. He, Z. Z. Zhang, L. Wu, Appl. Surf. Sci. **349**, 292 (2015).
[11] S. S. Hosseinpour-Mashkani, S. S. Hosseinpour-Mashkani, A. Sobhani-Nasab, J. Mater. Sci.-Mater. El. **27**, 4351 (2016).
[12] Y. N. Zhu, G. H. Zheng, Z. X. Dai, J. J. Mu, Z. F. Yao, J. Mater. Sci. Technol. **33**, 834 (2017).
[13] G. O. Yang, G. W. Yang, C. Q. Sun, W. G. Zhu, Small **4**, 1359 (2008).
[14] Y. J. Wang, H. Xu, C. Y. Shao, J. Cao, Appl. Surf. Sci. **392**, 649 (2017).
[15] Y. N. Zhu, G. H. Zheng, Z. X. Dai, L. Y. Zhang, Y. Q. Ma, J. Mater. Sci. Technol. **33**, 23 (2017).
[16] B. Zhou, X. Zhao, H. J. Liu, J. H. Qu, C. P. Huang, Sep. Purif. Technol. **77**, 275 (2011).
[17] H. Kato, A. Kudo, Phys. Chem. Chem. Phys. **2**, 2833 (2002).
[18] S. Ouyang, H. Tong, N. Umezawa, J. Cao, P. Li, Y. Bi, Y. Zhang, J. Ye, J. Am. Chem. Soc. **134**, 1974 (2012).
[19] Y. K. Yin, Y. Gao, Y. Z. Sun, B. B. Zhou, L. Ma, X. Wu, X. Zhang, Mater. Lett. **64**, 602 (2010).
[20] K. S. Aneesh Kumar, R. N. Bhowmik, Mater. Chem. Phys. **146**, 159 (2014).
[21] E. Çiftyürek, K. Sabolsky, E. M. Sabolsky, Sensor. Actuat. B-Chem. **237**, 262 (2016).
[22] J. T. Li, V. Maurice, J. Swiatowska-Mrowiecka, A. Seyeux, S. Zanna, L. Klein, S. G. Sun, P. Marcus, Electrochim. Acta **54**, 3700 (2009).
[23] T. Thongtem, S. Kungwankunakorn, B. Kuntalue, A. Phuruangratc, S. Thongtem, A. Phuruangratc, S. Thongtem, J. Alloy. Compd. **506**, 475 (2010).
[24] Y. Sun, J. F. Ma, J. R. Fang, C. Gao, Z. S. Liu, Inorg. Chem. Commun. **14**, 1221 (2011).
[25] R. Krishnan, J. Thirumalai, S. B. Thomas, M. Gowri, J. Alloy. Compd. **604**, 20 (2014).
[26] H. C. Lei, X. B. Zhu, Y. P. Sun, W. H. Song, J. Cryst. Growth **310**, 789 (2008).
[27] G. J. Xing, Y. M. Li, Y. L. Li, Z. L. Wu, P. Sun, Y. Wang, C. Zhao, G. M. Wu, Mater. Chem. Phys. **127**, 465 (2011).
[28] S. J. Lei, X. M. Peng, X. P. Li, Z. H. Liang, Y. Yang, B. C. Cheng, Y. H. Xiao, L. Zhou, Mater. Res. Bull. **46**, 601 (2011).
[29] Y. N. Zhu, G. H. Zheng, Z. X. Dai, L. Y. Zhang, J. J. Mu, J. Mater. Sci. Technol. **32**, 1361 (2016).
[30] J. Zhang, R. Li, L. Liu, L. Li, L. Zou, S. Gan, G. Ji, Ultrason. Sonochem. **21**, 1736 (2014).
[31] X. Liu, L. Li, H. M. Noh, B. K. Moon, B. C. Choi, J. H. Jeong, Dalton T. **43**, 8814 (2014).

[32] N. Niu, P. Yang, W. Wang, F. He, S. Gai, D. Wang, J. Lin, Mater. Res. Bull. **46**, 333 (2011).
[33] M. Ashokkumar, S. Muthukumaran, Powder Technol. **258**, 157 (2014).
[34] D. L. Wood, J. Tauc, Phys. Rev. B **5**, 3144 (1972).
[35] R. Lacomba-Perales, J. Ruiz-Fuertes, D. Errandonea, D. Martinez-Garcia, A. Segura Martinez-Garcia D, A Segura, Epl-Europhys. Lett. **83**, 226 (2008).
[36] J. C. Sczancoski, L. S. Cavalcante, M. R. Joya, J. A. Varela, P. S. Pizani, E. Longo, Chem. Engin. J. **140**, 632 (2008).
[37] M. Muralidharan, V. Anbarasu, A. E. Perumal, K. Sivakumar, J. Mater. Sci.-Mater. El. **27**, 2545 (2016).
[38] C. L. Yu, Z. Wu, R. Y. Liu, D. D. Dionysiou, K. Yang, C. Y. Wang, H. Liu, Appl. Catal. B-Environ. **209**, 1 (2017).
[39] D. L. Chen, M. Zhang, Q. J. Lu, J. F. Chen, B. T. Liu, Z. F. Wang, J. Alloy. Compd. **646**, 647 (2015).
[40] Y. F. Wang, X. Zhang, J. X. Liu, Y. W. Wang, D. H. Duan, C. M. Fan, Mater. Sci. Semicon. Proc. **40**, 613 (2015).
[41] X. D. Ma, D. L. Jiang, P. Xiao, Y. Jin, S. C. Meng, M. Chen, Catal. Sci. Technol. **7**, 3481 (2017).
[42] Z. F. Yao, G. H. Zheng, Z. X. Dai, L.Y.Zhang, Appl. Organometal. Chem. **4412**, 1 (2018).
[43] Y. H. Ng, A. Iwase, N. J. Bell, A. Kudo, R. Amal, Catal. Today **164**, 353 (2011).
[44] G. Tian, Y. Chen, X. Meng, J. Zhou, W. Zhou, K. Pan, C. Tian, Z. Ren, H. Fu, Chem. Plus Chem. **78**, 117 (2013).
[45] X. Bai, L. Wang, Y. Zhu, ACS Catal. **2**, 2769 (2012).